RSC Advances

PAPER

View Article Online
View Journal | View Issue

Cite this: *RSC Adv.*, 2016, **6**, 68028

Substitution driven structural and magnetic properties and evidence of spin phonon coupling in Sr-doped $BiFeO_3$ nanoparticles†

Sunil Chauhan,[a] Manoj Kumar*[a] and Prabir Pal[b]

The manifestation of dimensionalities and Sr induced modifications in structural, vibrational and magnetic properties of $Bi_{1-x}Sr_xFeO_3$; ($x = 0-0.25$) nanoparticles synthesized by a tartaric acid based sol–gel route are reported. X-ray diffraction and electron microscopy studies reveal the phase purity and nanocrystalline nature (45–90 nm) of $Bi_{1-x}Sr_xFeO_3$ samples. The Sr ions substitution motivated the coexistance of rhombohedral (*R*3*c*) and pseudo tetragonal (*P*4/*mmm*) structural symmetry for the $x = 0.25$ sample which leads to enhancement of saturation magnetization due to the distorted cycloid spin structure and uncompensated surface spins, which is in concomitance with the electron paramagnetic resonance (EPR) and Mössbauer studies. The ferromagnetic ordering contribution continuously increases with increasing Sr content from $x = 0-0.25$ samples with a maximum saturation magnetization of 0.72 emu g^{-1} for the $x = 0.25$ sample which is also endorsed by second order Raman modes. X-ray photoelectron and Mössbauer measurements confirmed the dominance of the Fe^{3+} oxidation state. Alteration in QS hyperfine parameters and line-width analysis have been probed by Mössbauer analysis with increasing Sr content in $BiFeO_3$ nanoparticles suggesting the destruction of the spin cycloid.

Received 28th April 2016
Accepted 8th July 2016

DOI: 10.1039/c6ra11021e

www.rsc.org/advances

1. Introduction

Over the past few years, multiferroics have captured great attention for their potential application in the emerging field of multifunctional devices. Multiferroics simultaneously possess ferroic properties, such as ferroelectricity, ferromagnetism and ferroelasticity, coupled with electric, magnetic and structural order parameters.[1–4] So far, several single-phase multiferroics have been developed such as $DyMnO_3$, $BiMnO_3$, $YMnO_3$ and $BiFeO_3$.[4] Among these multiferroics, $BiFeO_3$ is known to be the only room temperature multiferroic, which is a potential candidate for several applications in different fields such as electromagnetic wave attenuation, resistive switching, gas sensors, solar cells, oxygen photocatalytic and simultaneous multi-harmonic imaging of nanoparticles in tissues.[5–9] $BiFeO_3$ shows ferroelectricity (T_C = 826–845 °C) and antiferromagnetism (T_N = 370 °C) in single phase at room temperature and has rhombohedrally distorted perovskite structure with space group *R*3*c*, having rhombohedral lattice parameters $a_r = 5.63$ Å, $\alpha_r = 59.35°$, or alternatively, hexagonal parameters $a_{hex} = 5.58$ Å, $c_{hex} = 13.87$ Å.[4,5] In $BiFeO_3$, ferroelectricity arises due to stereochemically active $6s^2$ lone pair electrons of Bi^{3+} ions and it is displacive-type ferroelectric material.[3,4] In displacive-type ferroelectric materials, the most fundamental requirement is atomic displacement along the specific direction in their crystal structure to induce a spontaneous polarization. Bi^{3+} and Fe^{3+} cations are displaced along the hexagonal [001]-axis, leading to a spontaneous polarization in this direction. At the same time, magnetic moments of Fe^{3+} cations exhibit a canted antiferromagnetic G-type ordering with a small canting angle. The residual net magnetic moment of the canted antiferromagnetic state is canceled by a long-range modulated spin structure with a period length of about 62 nm. This long-range modulation can be modeled by cycloidal structure of Fe^{3+} magnetic moments with $[110]_{hex}$ as propagation vector and magnetic moments pointing in the plane defined by the cycloidal propagation and the polarization vector.[3,4] However, weak magnetic behavior and leakage currents in $BiFeO_3$ are main drawbacks for its applications.[4,5] Many current investigations seek to suppress the spiral spin structure in $BiFeO_3$ to enhance the magnetic properties and consequently to enhance the multiferroic properties. It is widely expected that the strategies based on decreasing the particle size (nanomaterials), divalent cations (Ba, Ca, Sr and Pb), transition metal ions (Ti, Nb, W, Co, Mn and Ni) and rare-earth metal ions Lanthanide series (R = Dy, Gd, Eu and Pr) substitution will have great impact on their magnetic, electric, optical and magnetoelectric properties.[10–17] Rare earth ions are magnetically active ions leading to the orthoferrites ($RFeO_3$) orthorhombic phase (ferromagnetic). It is difficult to measure the

[a]*Department of Physics and Materials Science & Engineering, Jaypee Institute of Information Technology, A-10, Sector-62, Noida-201307, India. E-mail: mkumar.phy@gmail.com*

[b]*Academy of Scientific and Innovative Research (AcSIR), CSIR-National Physical Laboratory (CSIR-NPL) Campus, Dr K S Krishnan Road, New Delhi 110012, India*

† Electronic supplementary information (ESI) available. See DOI: 10.1039/c6ra11021e

solubility limit and phase identification of the rare earth ions doped $BiFeO_3$ ceramics as discussed by D. C. Arnold.[15] Transition metal ions (Ti^{4+}, Nb^{5+} and W^{6+}) doped $BiFeO_3$ ceramics form the core@shell $BiFeO_3$@$Bi_{3-\delta}Fe_5O_{12}$ type microstructure and the impurity phase increases with increasing the transition metal aliovalancy.[14] Recently, significant efforts have been made to understand the effect of chemical substitution of Sr on the crystal structure and magnetic properties of $BiFeO_3$ ceramics.[18–24] The ionic radius of Sr^{2+} ion (1.26 Å, CN 8) is slightly larger than that of Bi^{3+} ion (1.17 Å, CN 8), which can lead to the lattice distortion in $BiFeO_3$ crystal. The Sr^{2+} ion is magnetically inactive and the distortion due to the ionic radii difference in crystal structure is expected to enhance the magnetization in $BiFeO_3$ even for small doping concentration. These changes affect the degree of off-centering of the FeO_6 octahedra and thus, also the multiferroic properties of $BiFeO_3$. Charge compensation for the substitution of Sr^{2+} for Bi^{3+} in $BiFeO_3$ ceramics could occur by the introduction of vacancies on oxygen sites or by oxidation of Fe^{3+} to Fe^{4+} giving solid solutions between $BiFeO_3$ and $SrFe^{3+}O_{2.5}$ or $SrFe^{4+}O_3$, respectively. Hussain *et al.* reported the pseudo cubic crystal structure and Fe ions are in trivalent state along with the oxygen deficiency in 25% Sr doped $BiFeO_3$ ceramics using the X-ray diffraction and Mössbauer spectroscopy results.[19] Bhushan *et al.* showed the rhombohedral structure with dominancy of Fe^{3+} ions in 0–7% Sr doped $BiFeO_3$ nanoparticles.[20] Kundys *et al.* reported the magnetic field induced polarization of $P_r = 96\ \mu C\ cm^{-2}$ at 10 T in $Bi_{0.75}Sr_{0.25}FeO_{3-\delta}$ ceramic is highest among the experimentally reported value for all previously reported $BiFeO_3$ based systems among thin films or bulk samples.[21] However there are several contradictory reports available on crystal structure and magnetic properties of Sr doped $BiFeO_3$ ceramics with respect to the role of the Fe oxidation state (Fe^{2+}, Fe^{3+} and Fe^{4+}) or/and coordination and crystal structures.[21–23] The structural, magnetic and ferroelectric properties of 50% Sr doped $BiFeO_3$ with rhombohedral crystal structure and Fe ions with +2 and +3 oxidation states have been reported by Balamurugan *et al.*[22] Contrarily, Li *et al.* found that Fe ions maintained a +3 state and the magnetization of the samples decreases with increasing Sr content which they attributed to the decrease in coordination of Fe^{3+} from octahedral to tetrahedral.[23] Mandal *et al.* with XPS analysis showed that Fe ions exhibited Fe^{3+} and Fe^{4+} state along with the presence of oxygen vacancies.[24] Furthermore, the increasing amount of oxygen vacancy would result in another interesting electrical conductive phenomenon *e.g.*, threshold switching (TS) effect which can be used in electronic devices.[25] Among the various reasons of incompleteness on the studies of $Bi_{1-x}Sr_xFeO_3$ system includes the different values of x. The other reasons (like dependence of sample properties) strongly depend on method of preparation (*i.e.* solid state or sol–gel route) and processing conditions.[18–24]

Previous structural and Mössbauer studies were carried out mostly on bulk-Sr doped $BiFeO_3$ samples to ravel structural transformation and its long-range ordering but few reports were available on Sr doped $BiFeO_3$ nanoparticles. SQUID (or VSM) magnetic measurements provided information on net magnetization, but no further insight into the spin structure of nanoparticles using Electron Paramagnetic Resonance studies were done. In this Communication, we present the detailed study of structural and magnetic properties of $Bi_{1-x}Sr_xFeO_3$ nanoparticles ($x = 0$, 0.05, 0.1, 0.15, 0.20 and 0.25). Nano-crystalline samples are prepared by modified sol–gel route and systematically investigated for changes in the crystallographic structure, microstructure and magnetic properties by using Rietveld analysis, TEM, Raman, XPS, VSM, EPR and Mössbauer techniques. The origin of the mixed rhombohedral and pseudo tetragonal structural state is elaborated with substitution induced lattice and octahedral distortions in a perovskite unit cell and the structural changes are correlated with magnetic properties. X-ray Photoelectron Spectroscopy (XPS) results confirmed the Fe^{3+} dominancy in Sr doped $BiFeO_3$ nanoparticles. Mössbauer spectroscopy results showed the distorted cycloidal spin structure in Sr doped $BiFeO_3$ nanoparticles.

2. Experimental details

2.1 Materials synthesis

Pure and Sr doped $BiFeO_3$ nanoparticles were prepared by tartaric acid modified sol–gel route. All chemical (Sigma) reagents used as starting materials were analytic grade and do not require additional purification treatment. In a typical sol–gel process for $BiFeO_3$ nanoparticles, calculated amounts of bismuth nitrate ($Bi(NO_3)_3 \cdot 5H_2O$) and ferric nitrate ($Fe(NO_3)_3 \cdot 9H_2O$) were dissolved in deionized water. As $Bi(NO_3)_3 \cdot 5H_2O$ undergoes decomposition into bismuth oxychloride in water, it was first taken in 50 ml deionized water and kept on stirring. During stirring dilute nitric acid was added drop by drop until a clear and transparent solution was obtained which confirmed the complete dissolution of $Bi(NO_3)_3 \cdot 5H_2O$ and then ferric nitrate solution was added. The stoichiometric amount of tartaric acid ($C_6H_6O_7$) was further added for complete combustion of the nitrates. In present report tartaric acid was used as chelating agent for the synthesis of Sr doped $BiFeO_3$ nanoparticles. It is difficult to obtain phase pure $BiFeO_3$ samples and several secondary phases (Bi_2O_3, $Bi_2Fe_4O_9$ and $Bi_{46}Fe_2O_{72}$) exist in the samples synthesized with citric acid as chelating agent. S. Gosh *et al.* and M. Arora *et al.* reported pure phase formation of $BiFeO_3$ nanoparticles by using tartaric acid as chelating agent.[26] The uniqueness of the tartaric acid as a chelating agent in synthesis of $BiFeO_3$ nanoparticles probably resides in the formation of hetero-metallic polynuclear complexes in the solution, where reacting metal atoms come in close proximity. This occurs because of the presence of two carboxylate and two hydroxyl groups with proper orientation to form a polynuclear complex, which breaks on heating in the presence of concentrated HNO_3 leading to the formation of pure phase $BiFeO_3$ samples. The yellow transparent solution was stirred vigorously for 12 h at 60 °C. Further the transparent solution was dried for two days in an oven maintained at 120 °C to get the fluffy gel. Finally, the fluffy gel was calcined at different temperatures 400, 500 and 600 °C for two hrs in an air ambience. Sr doped $BiFeO_3$ samples with different Sr doping concentrations were prepared by adding the calculated amount $Sr(NO_3)_2 \cdot 5H_2O$ in the precursor solution keeping all other experimental conditions invariant.

2.2 Characterization

The prepared samples were structurally characterized by X-Ray diffractometer (XRD-6000 Shimadzu). The measurements were carried out at room temperature using Cu K_α radiation source (λ = 1.5406 Å, operated at 40 kV and 30 mA) and the data was collected in the range $2\theta = 10°$ to 95° with the step size of 0.02° and 1.2 seconds count time at each step. Rietveld refinement analysis of the XRD patterns were performed with Program FullProf (Version 3.00-June 2015). Si sample has been used as an external standard to deconvolute the contribution of instrumental broadening. The instrumental parameters were kept constant during the fitting. Program refinement of the first sample was started with the space group *R3c* with O at 18b-site, Bi at 6a-site and Fe at 6a-site and the global parameters were refined in the first step. In the next step, the structural parameters such as lattice parameter, atomic coordinates and site occupancy were refined. The fitting quality of the experimental data was checked by using the goodness of fitting parameter (χ^2). Scanning electron microscopic images were recorded by using a Zeiss Ultra Plus field-emission scanning electron microscope (FESEM) operated at 10 kV. The TECNAI with LaB_6 electron source was used for High Resolution Transmission Electron Microscope (HRTEM) operated at 200 kV to image pure and Sr doped $BiFeO_3$ nanoparticles. The samples for the TEM analysis were prepared by placing a drop of dilute suspension of nanoparticles on carbon coated copper grid. Raman spectroscopy was carried out in the backscattering configuration (LabRAM HR) with charge coupled device detector and 514.5 and 785 nm laser excitation sources. The laser power was kept below 2 mW in order to avoid any sample heating. The X-ray photoelectron spectroscopy (XPS) measurements were performed by using an Omicron μ-metal ultrahigh vacuum (UHV) system equipped with a monochromatic Al K_α X-ray source ($h\nu = 1486.6$ eV) and a multi-channeltron hemispherical electron energy analyzer (EA 125). The C 1s core levels were measured throughout the experiment particularly before and after each XPS spectra. The samples were heated *in situ* at 300 °C under ultra high vacuum conditions and then cooled down to room temperature before photoemission measurements. This heating procedure helped us to clean the sample surface. The photoemission measurements were performed in the analysis chamber under a base vacuum of $\sim 5.0 \times 10^{-11}$ mbar at room temperature. The room temperature magnetic measurements of samples were carried out using vibrating sample magnetometer (Lakeshore VSM 7410). The magnetic resonance spectra were recorded with an electron paramagnetic resonance (EPR) spectrometer (JES FA200 CW ESR Spectrometer) using X-band gun diode. The samples were rolled into cylindrical shapes by wrapping them in Teflon tapes. These samples were stuffed into a quartz capillary tube. The sample was placed at the centre of the resonant cavity between pole caps of an electromagnet. The magnetic field was scanned from 0–800 mT, while the resonance frequency (~9.46 GHz) of the sample cavity was locked. Mössbauer effect measurements were carried out by using a standard PC-based spectrometer equipped with a Weissel velocity drive operating in the constant acceleration mode.

3. Result and discussion

3.1 X-ray diffraction analysis

Fig. 1(a) illustrates the X-ray diffraction patterns of $BiFeO_3$ samples sintered at 400, 500 and 600 °C respectively. It has been clearly observed that there is no $BiFeO_3$ diffraction peak except amorphous phase ($2\theta \sim 30°$) in the sample sintered at 400 °C. With increasing the sintering temperature to 500 °C, the XRD pattern expectedly shows the typical peaks of rhombohedral structure (JCPDS card number 71-2494) indicates the presence of crystalline $BiFeO_3$ ceramics.[27,28] With further increasing the sintering temperature to 600 °C, the intensities of $BiFeO_3$ diffraction peaks are found to increase suggesting improved nature of crystallization. Fig. 1(b) shows the X-ray diffraction patterns and its magnified view (near $2\theta \sim 32°$ and 39.5°) for $Bi_{1-x}Sr_xFeO_3$ (x = 0–0.25) samples sintered at temperature 600 °C. Diffraction peaks (104) and (110) are clearly separated for x = 0.0 sample (pure $BiFeO_3$), however, on increasing Sr content from x = 0.05 to 0.25, doublet (104) and (110) merged to a single peak. Moreover, (113) and (006) peaks are suppressed with increasing Sr content. Although ionic size of Sr^{2+} (1.26 Å) is greater than Bi^{3+} (1.17 Å) and we may expect an increase of the lattice constant and consequent decrease of 2θ with increasing Sr content, but the converse effect has been observed. All the diffraction peaks shift towards higher angles with increasing Sr^{2+} content up to x = 0.20 samples indicating decrease in the unit cell volume. However, for x = 0.25 sample the diffraction peaks (104) and (110) merge to a single peak indicating the signature of structural phase transformation. Merging, suppression and shifting of XRD peaks indicate that Sr doping in $BiFeO_3$ samples results in compressive lattice distortion which leads to evolution of pseudo-tetragonal *P*4/*mmm* phase. For detailed structural analysis, the Rietveld refinement of $Bi_{1-x}Sr_xFeO_3$; (x = 0–0.20) samples were carried out by considering the rhombohedrally distorted perovskite structure with *R3c* space group. The Bragg peaks are modeled with Thompson–Cox–Hastings pseudo-Voigt function and the background is estimated by linear interpolation between selected background points. The refinement of the structural parameters is continued till convergence is reached with goodness of fit (GoF) around 1.0.[29] Refinement of $Bi_{0.75}Sr_{0.25}FeO_3$ sample was performed using the same *R3c* structural model. However, the value of the goodness of fitting parameter (χ^2) was poor and the overall difference between the observed and calculated profiles was rather large. Careful verification of the profile fitting revealed the existence of extra reflections of low intensity corresponding to a pseudo-tetragonal *P*4/*mmm* phase which is typical of $SrFeO_3$-type ferrites.[30] This implies that the diffraction profile of x = 0.25 sample might be a result of superposition of two phase contributions rhombohedral *R3c* and pseudo-tetragonal *P*4/*mmm*. Using a bi-phasic (*R3c* + *P*4/*mmm*) model, stable refinement ($\chi^2 = 1.86$) with the major contribution from the rhombohedral phase (65.25%) and minor contribution from the phase with pseudo-tetragonal *P*4/*mmm* (34.75%) symmetry are obtained. The Rietveld refined XRD patterns for selected samples are shown in Fig. 1(c–f). The various parameters for all

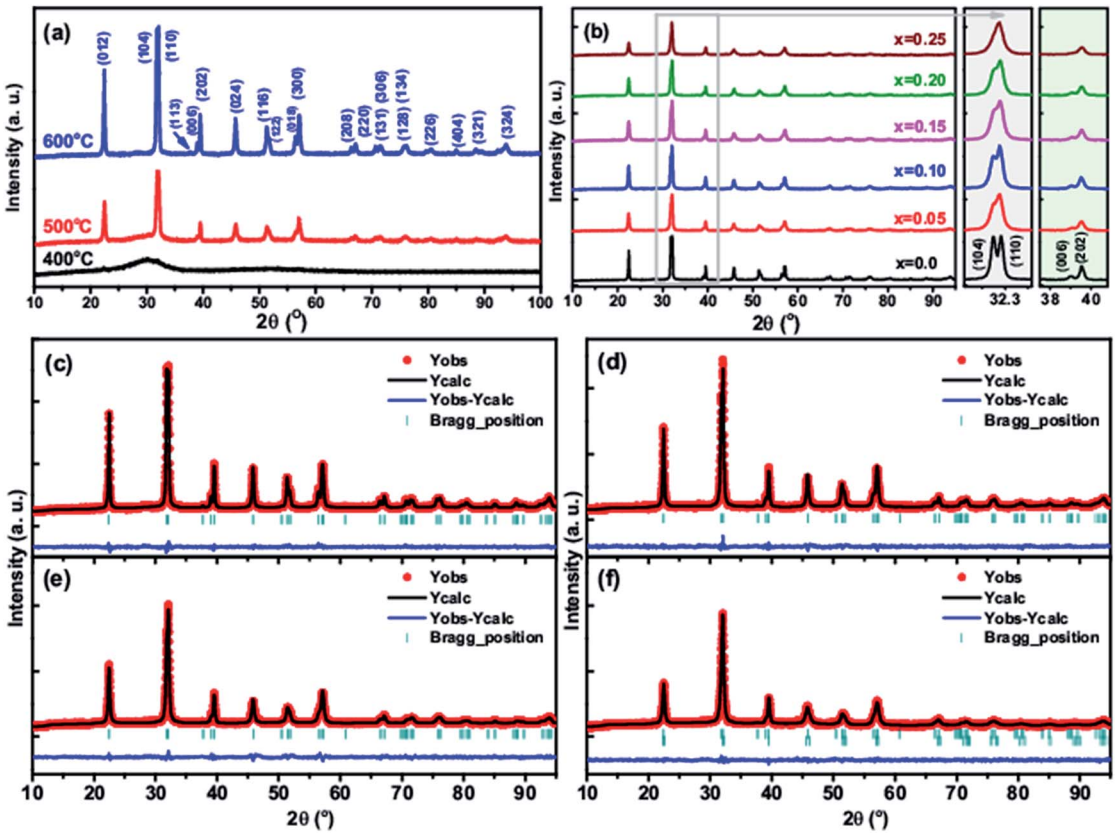

Fig. 1 (a) XRD patterns of $BiFeO_3$ precursor gel sintered at different temperatures. (b) XRD patterns of $Bi_{1-x}Sr_xFeO_3$ nanoparticles sintered at 600 °C. Rietveld refined XRD patterns of $Bi_{1-x}Sr_xFeO_3$ nanoparticles, (c) $x = 0.0$, (d) $x = 0.10$, (e) $x = 0.20$ and (f) $x = 0.25$.

the samples obtained from refinement of XRD patterns are listed in ESI Table S1.† The crystal structure of pure $BiFeO_3$ (*R3c*), $Bi_{0.8}Sr_{0.2}FeO_3$ (contracted *R3c*) and $Bi_{0.75}Sr_{0.25}FeO_3$ (*R3c* + *P4*/*mmm*) generated by refined ionic positions obtained from Rietveld refinement are shown in Fig. 2(a–c). The variation in the lattice constants "*a*" and "*c*" and cell volume "*V*" as a function of Sr content *x* are given in Table S1.† The unexpected decrease in the lattice constant with increasing Sr content is most likely an indicator of an increase in the concentration of oxygen vacancies due to the need for charge compensation. Li *et al.* have also reported a decrease in the lattice constant in Sr substituted $BiFeO_3$ compounds.[23]

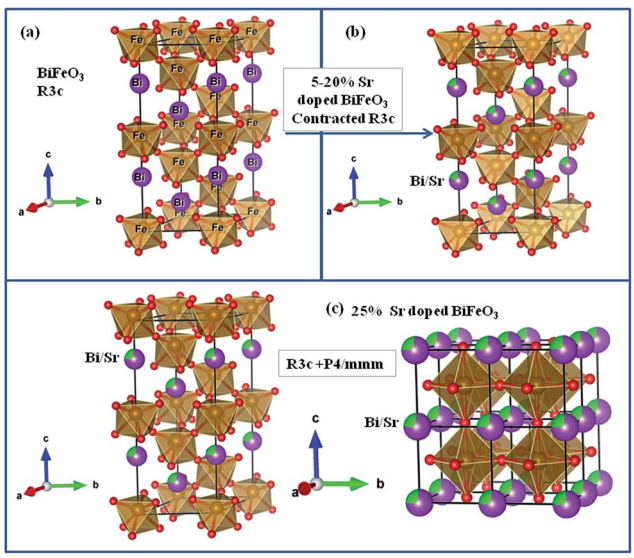

Fig. 2 (a) Rhombohedral perovskite *R3c* structure for pure $BiFeO_3$, (b) contracted rhombohedral perovskite *R3c* structure for 5–20% Sr doped $BiFeO_3$ and (c) rhombohedral perovskite *R3c* + pseudo tetragonal *P4*/*mmm* structure for 25% Sr doped $BiFeO_3$ (representation is based on the refined ionic positions obtained from Rietveld refinement).

Bond valence sum (BVS) rule gives the information whether the crystal is non-strained perfect or strained. In perfect crystal the formal charge of the cation (anion) is equal to the sum of the bond valences around this cation (anion) according to BVS. This rule is satisfied only if the stress introduced by the coexistence of different structural units can be relieved by the existence of enough degrees of freedom in the crystallographic structure.[31] The departure from the BVS rule is, therefore, a measure of the existing stress in the bonds of the structure. The bond valences calculated for Bi, Sr and Fe cations from the Bi/Sr–O and Fe–O bond distances are enlisted in ESI Table S2.† The BVS sum of Sr cation increases from 2.81 to 3.62 with increasing Sr content from 5% to 25%, higher than the expected in this compound. Fe cations exhibit valences of around 2.9 slightly lower than the expected. These results indicate the Sr cations are over-bonded and Fe cations are under-bounded in this structure. In other words Sr–O bonds are under compressive stress and Fe–O

bonds are under tensile stress giving rise to a structure with a relatively high metastable character.

3.2 FESEM and TEM analysis

The morphological analyses of the synthesized samples were done by the field emission scanning electron microscopy (FESEM) technique. FESEM micrographs for $x = 0.0$, 0.15 and 0.25 samples are shown in Fig. 3(a–c). FESEM images indicate that the synthesized pristine $BiFeO_3$ and $Bi_{1-x}Sr_xFeO_3$ ($x = 0.15$ and 0.25) samples have dense morphology of spherical grains with size ranging between 45 and 90 nm. Elemental analysis in these samples was carried out by using the EDS spectra. Typical EDS patterns of pristine $BiFeO_3$ and $Bi_{1-x}Sr_xFeO_3$ ($x = 0.15$ and 0.25) samples are shown in Fig. 3(d–f). The chemical composition of pristine $BiFeO_3$ agrees with the nominal composition: 1 : 1 : 3 approximately. Besides the obvious signals for O, Bi and Fe, the EDS spectra show a weak signal of Sr for $x = 0.15$ and 0.25 samples. The measured quantitative values yield atomic percentages of Bi, Sr and Fe are 18.03%, 16.66% and 1.14%, respectively, for $x = 0.15$ sample and 18.20%, 15.82% and 3.35%, respectively, for $x = 0.25$ sample. This showed that Sr ions were effectively incorporated into the host material.

Shape, size, lattice interplaner spacing and crystallinity of the synthesized nanostructured samples were further studied by using HRTEM technique. The TEM images of $Bi_{1-x}Sr_xFeO_3$ samples with $x = 0.0$, 0.15 and 0.25 are shown in Fig. 4(a–c), respectively. It is evident that spherical nanoparticles of size around 45–90 nm are observed for $x = 0.0$, 0.15 and 0.25 samples. It can be noticed that particle size decreases with increasing Sr concentration in $BiFeO_3$. The lattice strain due to ionic size mismatch between Sr and Bi, enhances the rate of nucleation and reduces the particle growth. The selected area electron diffraction (SAED) pattern of $Bi_{0.85}Sr_{0.15}FeO_3$ sample is also shown in Fig. 4(d). The diffraction pattern comprising of discrete rings indicates the polycrystalline nature of the sample. The simulated rings pattern for $Bi_{0.85}Sr_{0.15}FeO_3$ sample with the intensity of diffraction peaks is also shown in Fig. 4(d). Fig. 4(e) clearly shows the lattice interplaner spacing of $Bi_{0.85}Sr_{0.15}FeO_3$ nanoparticles which indicates that fine nanoparticles are well crystallized. The Fast Fourier Transform (FFT) using Gatan

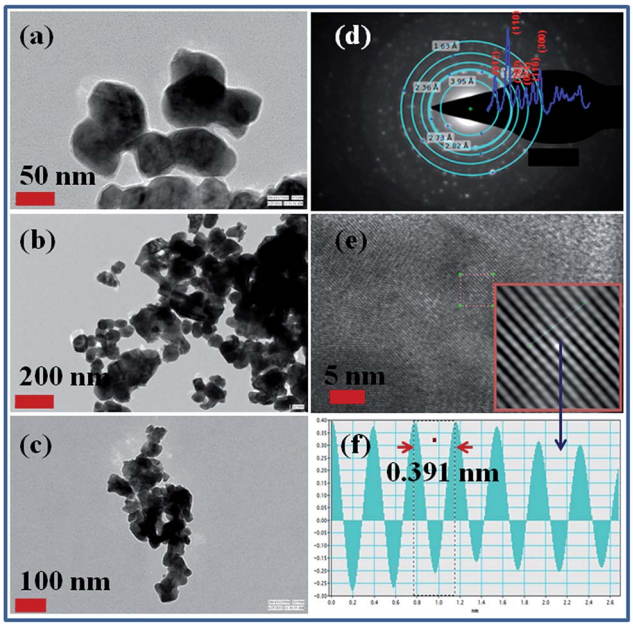

Fig. 4 TEM images of $Bi_{1-x}Sr_xFeO_3$ nanoparticles (a) $x = 0.0$, (b) $x = 0.15$, (c) $x = 0.25$, (d) selected area diffraction pattern for $x = 0.15$ nanoparticles with simulated ring pattern. (e) High resolution TEM image for $x = 0.15$ nanoparticles; the inset represents the fast Fourier transform (FFT) of the image, (f) the FFT was used to measure the interplanar distance corresponding to (012) plane.

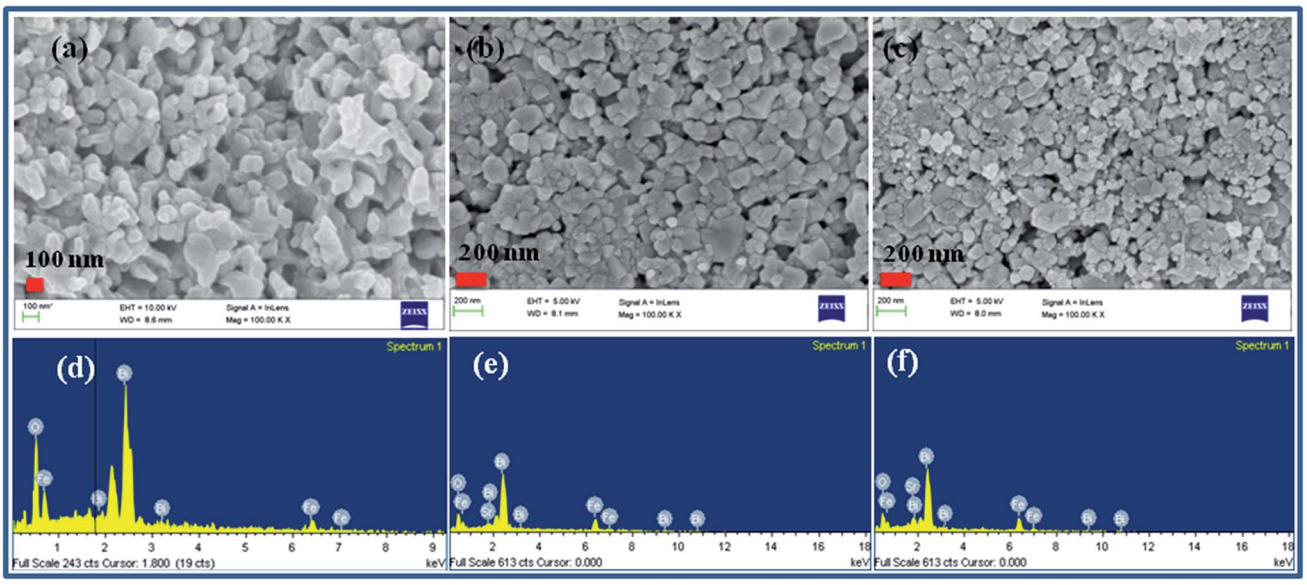

Fig. 3 FESEM micrographs of $Bi_{1-x}Sr_xFeO_3$ nanoparticles, (a) $x = 0.0$, (b) $x = 0.15$ and (c) $x = 0.25$. Typical EDS patterns of $Bi_{1-x}Sr_xFeO_3$ nanoparticles, (d) $x = 0.0$, (e) $x = 0.15$ and (f) $x = 0.25$.

Microscopy Suite software has been employed to measure the interplaner spacing and the FFT image is shown in the inset of Fig. 4(e). Fig. 4(f) shows the lattice plane intensity profile corresponding to Fig. 4(e), confirming the interplaner spacing of 0.391 nm corresponding to (012) plane of the $Bi_{0.85}Sr_{0.15}FeO_3$ nanoparticles.

3.3 Raman analysis

Fig. 5(a) shows the room temperature Raman spectra in the range 50–1500 cm^{-1} for $Bi_{1-x}Sr_xFeO_3$ (x = 0–0.25) nanoparticles. The assignment of observed Raman modes of distorted rhombohedral perovskite structure of $BiFeO_3$ with space group *R3c* is based on first principal calculations carried out by Hermet *et al.*[32] and experimentally reported FTIR data by Chen *et al.*[33] and Raman data by Porporati *et al.* and Bielecki *et al.*[34,35] The fitted Raman spectra for $Bi_{1-x}Sr_xFeO_3$ (x = 0.0, 0.15 and 0.25) nanoparticles are shown in Fig. 5(b)–(d), respectively. The observed modes position and FWHM of E and A modes for $Bi_{1-x}Sr_xFeO_3$ (x = 0–0.25) nanoparticles are summarized in ESI Table S3.† First Raman active mode near 75 cm^{-1} splits into two modes $E(TO_1)$ and $E(LO_1)$. Similarly both LO and TO modes are present for E(8) and E(9). The Raman modes doublet $E(TO_1)$, $E(LO_1)$ near 75 cm^{-1}, $E(TO_2)$ mode at 139.2 cm^{-1} and $A_1(TO_1)$ mode at 172.3 cm^{-1} are due to the displacement of Bi atoms due to the activation of lone pair $6s^2$ electrons of Bi^{3+} along the *c*-axis of hexagonal unit cell. The shifting of the first order modes $E(LO_1)/E(TO_1)$ with increasing the Sr content in $BiFeO_3$ samples is associated with strain *via* phonon deformation potentials α, β and γ,

$$\Delta\omega_E = \alpha(\varepsilon_{xx} + \varepsilon_{yy}) + \beta(\varepsilon_{zz}) + \gamma(\varepsilon_{xx} - \varepsilon_{yy}),$$

where ε_{xx}, ε_{yy} are the normal strains in the plane and ε_{zz} in the *c*-axis direction, respectively.[36,37] The suppression and shifting of Raman mode $E(TO_2)$ related to Bi–O bond towards the higher wavenumber with increasing the Sr content in $BiFeO_3$ is an indication of structural phase transition from rhombohedral to tetragonal.[38] The other interesting feature of the Raman spectra is the change in the intensity of $A_1(TO_1)$ mode in comparison with the $E(TO_1)$, $E(LO_1)$ and $E(TO_2)$ with increasing the Sr content in $BiFeO_3$ samples, which is an evidence for the spin dependent scattering mechanism with the magnetic anisotropy.[37] In the case of magnetically ordered system, the intensity of the Raman mode can be given by the relation,

$$I = |R + M\langle S_iS_j\rangle/S^2|^2$$

where R is the spin independent part, M is the magnetic moment, $\langle S_iS_j\rangle/S^2$ is the nearest neighbor spin correlation function.[37,39] The enhancement of $A_1(TO_1)$ intensity in comparison with the $E(TO_2)$ with increasing the Sr content in $BiFeO_3$ is due to different to the spin reorientation transitions with increasing the Sr content in $BiFeO_3$ samples. The next mode with $A_1(TO_2)$ symmetry at 218.4 cm^{-1} is soft oxygen mode and is related with the $a^-a^-a^-$ oxygen displacement vector.[32]

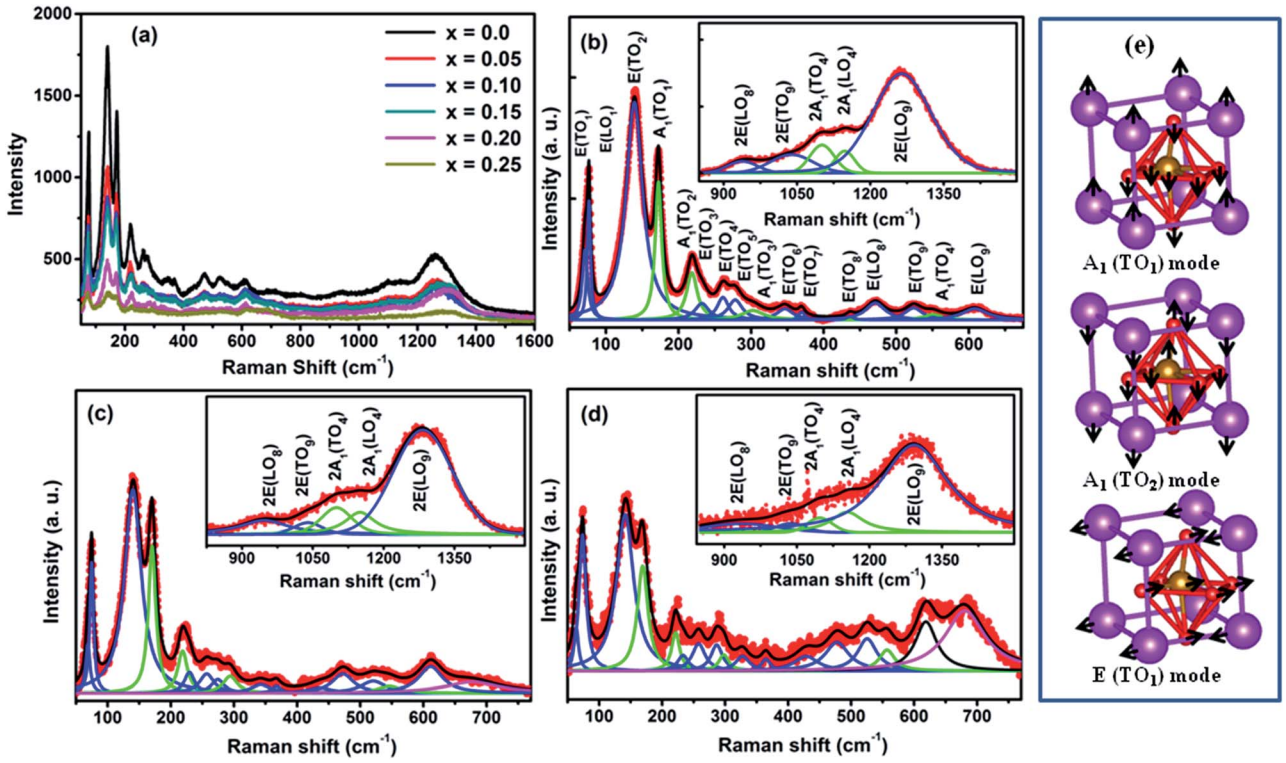

Fig. 5 (a) Raman spectra of $Bi_{1-x}Sr_xFeO_3$ nanoparticles at room temperature. (b) Deconvoluted first order Raman modes for x = 0.0. Inset shows the second order modes for x = 0.0. (c) Deconvoluted first order Raman modes for x = 0.15. Inset shows the second order modes for x = 0.15. (d) Deconvoluted first order Raman modes for x = 0.25. Inset shows the second order modes of for x = 0.25. (e) Illustrations show the A_1 and E vibration normal modes.

The $A_1(TO_1)$ and $A_1(TO_2)$ modes are associated to the structural distortions in comparison with the ideal cubic perovskite structure with space group $Pm\bar{3}m$. Fig. 5(e) illustrates the A_1 and E vibration modes. The change in the position and FWHM of the modes with increasing the Sr content in $BiFeO_3$ indicated the lattice distortion.

The second-order Raman phonon modes of $Bi_{1-x}Sr_xFeO_3$ (x = 0.0, 0.15, 0.25) nanoparticles are shown in the inset of Fig. 5(b)–(d), respectively. There are five vibrational modes from 900 cm^{-1} to 1400 cm^{-1}. These second-order modes labeled as $2E(LO_8)$, $2E(TO_9)$, $2A_1(TO_4)$, $2A_1(LO_4)$ and $2E(LO_9)$ are the combination modes and overtones produced by the first-order modes positioned between 450 and 630 cm^{-1}.[35,40,41] These second order phonon modes are assigned to long and short Fe–O (defined as Fe–O1 and Fe–O2) bond, respectively, where O1 are axial and O2 are equatorial ions.[41] The Fe–O2 is related to the octahedral rotation critical to weak ferromagnetic behavior in $BiFeO_3$. The structural distortion due to Sr doping should influence Raman modes due to the spin phonon coupling in these samples. The intensity of second order phonon modes of Sr doped $BiFeO_3$ samples decreases as compared to pure $BiFeO_3$ sample indicating the change in rotation of oxygen octahedral critical to weak ferromagnetism through superexchange interaction.[41] The variation of intensity of these second overtones predicts that magnetization might enhance with Sr content in $BiFeO_3$, indicating the spin-two phonon coupling in these samples. The second order phonon peaks are associated with the strong spin lattice coupling arising from the interaction between the adjacent magnetic sublattices.

Fig. 6(a–c) shows the Raman scattering spectra of the $Bi_{1-x}Sr_xFeO_3$ (x = 0.05, 0.15 and 0.25) nanoparticles, using two laser sources with different energy values (2.41 eV and 1.58 eV). Using 514.5 nm (2.41 eV) laser source, which is around 0.2 eV higher than the band gap value, the intensity of the second order phonon modes at 1255 cm^{-1} is of the same order as that of the corresponding fundamental modes.[20,42] The intensity of the second order modes around 1255 cm^{-1}, observed by using the laser source of 785 nm (1.58 eV). Laser source, is negligible because it does not have enough energy for direct and indirect electronic transitions. Another remarkable finding by using 514.5 nm and 785 nm laser sources is a notable intensity variation of the fundamental modes ~218 cm^{-1}. It is important to mention that the intensity variations observed in some vibrational modes are exclusively related to the atoms taking part in the electronic transition in the resonance Raman phenomenon.[42] In $BiFeO_3$ ceramics, the top of the valence band is composed of strong hybridization among O 2p and Bi 6p and also the bottom of the conduction band comprises of Fe 3d states. The optical band gap of the $BiFeO_3$ ceramics is due to the hybridization between the Fe 3d and O 2p states.[43] The Raman mode ~218 cm^{-1} is related to the Fe (3d) atoms. These facts could mean that when the energy of the laser source is sufficient to promote an-electronic transition from the valence band to the lower conduction band in $BiFeO_3$, a perturbation occurs in the electronic density of the 3d orbitals of the Fe atoms.[42] It consequently changes the polarizability of iron atoms resulting in enhancement of the intensity of 218 cm^{-1} mode. These

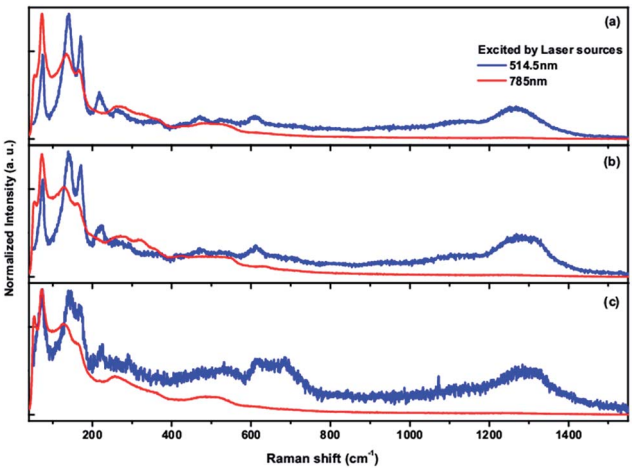

Fig. 6 Raman spectra of $Bi_{1-x}Sr_xFeO_3$ sample employing two different lasers as excitation source at room temperature, (a) x = 0.05, (b) x = 0.15 and (c) x = 0.25.

results confirm that electronic transitions take place under excitation with 514.5 nm laser radiations, allowing the resonance effect.

3.4 X-ray Photoelectron Spectroscopy (XPS) analysis

In order to identify the elements, chemical shift, oxidation state of elements and oxygen vacancies of the Sr doped $BiFeO_3$ samples, detailed XPS analysis has been carried out. The XPS survey spectra of the $Bi_{1-x}Sr_xFeO_3$ (x = 0.15 and 0.20) samples are presented in Fig. 7. The XPS survey spectra reveal the presence of Bi, Fe, O, and Sr without any other trace impurities except for a small amount of carbon. This confirms the chemical compositions of the Sr doped $BiFeO_3$ samples. For narrow scan spectra, the core level C 1s (285.0 eV) peak is taken as a reference for the calibration of the binding energy values obtained for the elements. The narrow scan XPS spectra of Bi 4f, Fe 2p, Sr 3d and O 1s lines for $Bi_{1-x}Sr_xFeO_3$ (x = 0.20 and 0.25) samples are shown in Fig. 8. Fig. 8(a) shows that Bi 4f doublet consisting of two peaks at 158.43 and 163.75 eV, which are from Bi–O bonds. The moderate shifting of Bi 4f peaks towards the higher binding energy with increasing x indicates the substitution of Sr^{2+} ions at Bi^{3+} sites in $BiFeO_3$ lattice. The chemical shift in Bi $4f_{7/2}$ and Bi $4f_{5/2}$ peaks arises due to variation in electro-negativity of Bi, Sr, Fe and O elements. The covalency/ionicity of Bi–O, Sr–O and Fe–O bonds have been calculated for x = 0.15 and 0.20 samples. The fraction of covalency (F_c) is estimated from the difference in anion and cation electronegativity values (ΔE_N) as: $F_c = \exp(-(\Delta E_N)^2/4)$, while the fraction of ionicity is calculated by: $F_i = (1 - F_c)$.[44,45] According to the electronegativity values of Bi, Sr, Fe and O elements, the F_c and F_i values for Bi–O, Sr–O and Fe–O bonds are calculated. The fraction of ionicity (F_i) for Sr–O bond (0.79) is much larger than that for Bi–O bond (0.40). This indicates that the bonding energy of (Bi/Sr–O) bond in the oxygen octahedron would be larger than that of pure Bi–O bond which results in slight shifting of 4f peaks towards the higher binding energy side with

increasing Sr content in $BiFeO_3$ samples. Fig. 8(b) shows Fe 2p XPS core spectra of $Bi_{1-x}Sr_xFeO_3$ samples with $x = 0.15$ and 0.20. The Fe 2p doublet consists of two wide peaks of Fe $2p_{3/2} \sim 710.13$ eV and Fe $2p_{1/2} \sim 723.45$ eV for $x = 0.15$, which are mainly ascribed to Fe–O bonds. Spin–orbit splitting energy is equal to 13.32 eV, which is comparable to the theoretical value of Fe 2p (13.6 eV) for Fe_2O_3.[44,45] The Fe $2p_{1/2}$ peak for Fe^{3+} oxidation state is 13.41 eV above the Fe $2p_{3/2}$ peak which appeared around 709.76 eV for $x = 0.20$ sample. In general, satellite peak appears at 8 eV above $2p_{3/2}$ for Fe^{3+}. In both samples, a satellite peak is observed at ~7.5 eV above Fe $2p_{3/2}$, which confirms the dominant 3+ oxidation state of Fe. According to the fitting, the compositional ratio of Fe^{2+} : Fe^{3+} is calculated as 27.8 : 72.2 and 35.4 : 64.6 for $x = 0.15$, 0.20 respectively. The Sr 3d spectra deconvoluted into two wide peaks of Sr $3d_{5/2} \sim 346.26$ eV, Sr $3d3_{/2} \sim 349.81$ eV and the broad hump (solder) – due to the SrO for $x = 0.15$, 0.20 are shown in Fig. 8(c), which are mainly ascribed to Sr–O bonds.[46] Fig. 8(d) shows the O 1s peak is de-convoluted into three peaks; the lower binding (LB) energy, medium binding (MB) energy and higher binding (HB) energy for $x = 0.15$, 0.20 samples. These peaks are attributed to the oxygen present in the lattice, oxygen loss and absorbed oxygen on the surface, respectively. The percentage of the oxygen vacancy concentration is found to be 12.3%, 16.2% for $x = 0.15$, 0.20, respectively, as calculated by the ratio of MB/(LB + MB + HB). In order to study the evolution of valence band (VB) states in $Bi_{1-x}Sr_xFeO_3$ samples with $x = 0.15$ and 0.20, we have measured the XPS VB spectra as shown in Fig. 9. A localized peak between 11 and 14 eV binding energy shown in Fig. 9, arises predominantly from Bi 6s states. The broad peak between 2 and 9 eV binding energy observed in both samples is generally attributed to hybridized Fe 3d–O 2p states with a considerable amount of Bi 6p character.[47,48] From these data, we have estimated the separation between the valance band maxima (E_{VBM}) and the Fermi energy (E_F) to be 0.90 eV ($x = 0.15$) and 1.03 eV ($x = 0.20$) for $Bi_{1-x}Sr_xFeO_3$ samples (inset of Fig. 9).[49] The position of the valence band maxima (E_{VBM}) has been determined from the extrapolation of two linear fits of leading edge and base line. It can be seen that the position of E_{VBM} is slightly shifted away from the Fermi level with increasing Sr ion content. Consequently, the XPS results demonstrate that the Sr doping leads to an enhancement of the oxygen vacancy concentration. The increased concentration of oxygen vacancies modulates the energy of the E_F and thus modulates the optical band gap and electrical properties.

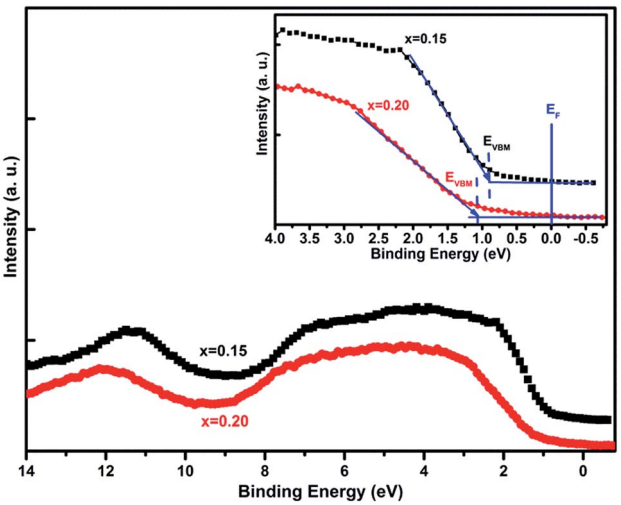

Fig. 9 XPS valence-band spectra of $Bi_{1-x}Sr_xFeO_3$ samples. Inset shows the magnified view.

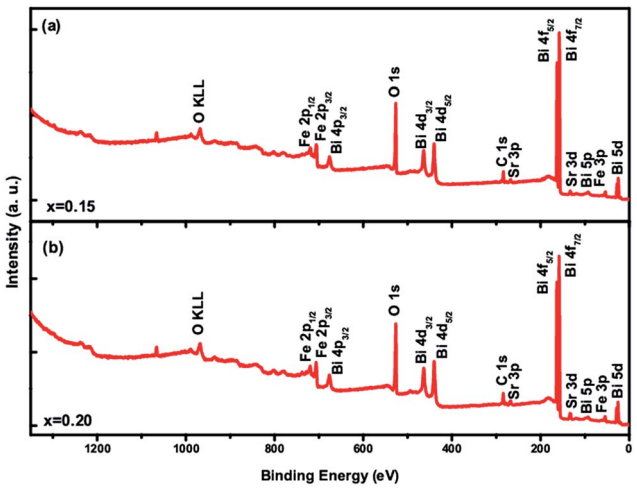

Fig. 7 XPS survey spectra of the of $Bi_{1-x}Sr_xFeO_3$ samples, (a) $x = 0.20$ and (b) $x = 0.25$.

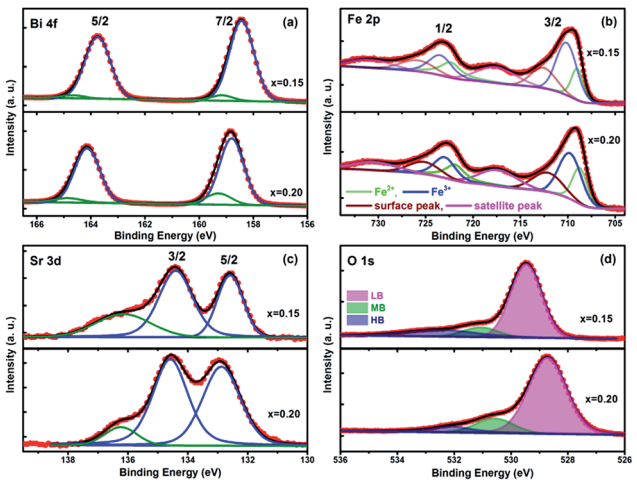

Fig. 8 Deconvoluted core level XPS spectra of (a) Bi 4f, (b) Fe 2p, (c) Sr 3d and (d) O 1s lines $Bi_{1-x}Sr_xFeO_3$ samples with $x = 0.15$ and 0.20.

3.5 Vibrating Sample Measurement (VSM) analysis

Magnetic measurements of prepared samples were recorded to study the effect of Sr doping on magnetic properties of $BiFeO_3$ nanoparticles. The magnetic hysteresis (M – H) loops for $Bi_{1-x}Sr_xFeO_3$ samples are shown in Fig. 10(a). The antiferromagnetic (AFM) and weak ferromagnetic (WFM)

M − H curves consists two parts that are paramagnetic (PM) and ferromagnetic (FM). In order to separate out ferromagnetic and paramagnetic contributions in M − H hysteresis loops, the M − H loops were analyzed by the following equation:

$$M(H) = 2\frac{M_{FM}^{S}}{\Pi}\tan^{-1}\left[\frac{H \pm H_{ci}}{H_{ci}}\tan\left\{\frac{\Pi M_{FM}^{R}}{2M_{FM}^{S}}\right\}\right] + \chi H.$$

The first term demonstrates the ferromagnetic part and the second term represents the linear contributions from AFM and/or PM part.[42,50] The fitted M − H curve along with FM and PM parts for $Bi_{1-x}Sr_xFeO_3$: $x = 0.0$, 0.15 and 0.25 samples are shown in Fig. 10(b–d) and the parameters obtained from fitting are listed in Table 1. The obtained parameters agree with the canted antiferromagnetic order of $BiFeO_3$ ceramics and are comparable with the reported values.[51,52] Park *et al.* demonstrated that the weak ferromagnetic response in $BiFeO_3$ can be initiated when the size of the nanoparticles is less than 95 nm.[11,51,52] The magnetic response increases rapidly with decreasing the size of the nanoparticles below 62 nm, the period length of spiral spin structure. From the TEM measurements, it was confirmed that size of Sr doped $BiFeO_3$ nanoparticles varies in the range 45–90 nm, in decreasing order with increasing Sr content. The antiferromagnetic materials contain two spin sublattices, with ferromagnetic interaction within each sublattice and antiferromagnetic interaction in the inter-sublattices. This two sublattices model leads to long-range collinear antiparallel spin structure with zero net magnetic moment due to complete spin compensation between these two sublattices. Moreover, incomplete spin compensation between these two sublattices can also occur in antiferromagnetic materials.[11] In nano-sized antiferromagnetic materials, long-range antiferromagnetic ordering often gets disturbed at the particle surface. Hence, in antiferromagnetic materials, if resultant small magnetic moment is observed, it could be due to the presence of uncompensated spins in the two sublattices. In addition, the higher surface-to-volume ratio in nanoparticles results in uncompensated spins at the surface and enhanced magnetization (due to disturbed antiferromagnetic ordering). It can be observed from the fitted MH loops that ferromagnetic ordering contribution increases with increasing Sr content and is maximum for $x = 0.25$ sample. The contribution of paramagnetic component increases continuously with increasing Sr doping. The elementary idea of DM interaction is the induction of magnetization in antiferromagnets due to the modification in 'canted' spins as a result of the ferroelectric distortions. Therefore, it can be suggested that the improved magnetic ordering in $Bi_{1-x}Sr_xFeO_3$ samples is due to the modifications in its 'canted' spin structure (Fe–O–Fe) which leads to the enhanced magnetic properties as illustrated in Fig. 10(e). With Sr substitution, structural distortion occurs that results in the canting of spins and therefore the bond angle of Fe–O–Fe changes from 156.8° to 146.9°, calculated using BondSTR (FULLPROF) shown in Table S2.†[43,53] These canted spin antiferromagnetic ordering in Sr doped $BiFeO_3$ nanoparticles are further explained in EPR studies.

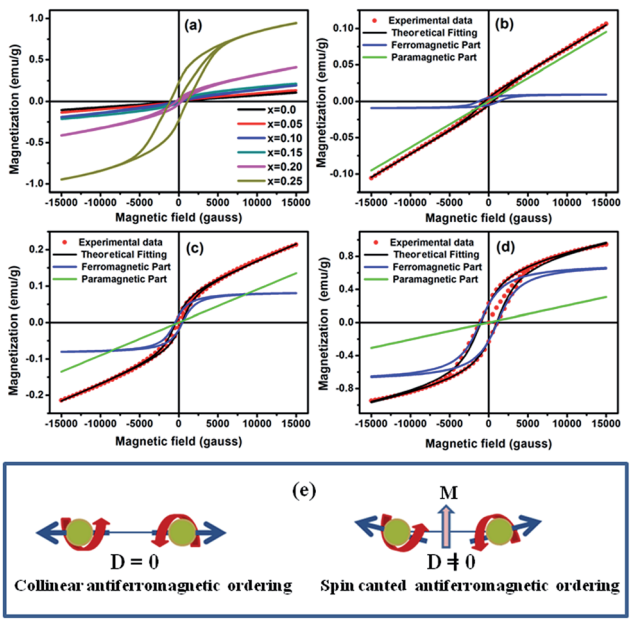

Fig. 10 (a) Magnetization *versus* magnetic field (M − H) curves for $Bi_{1-x}Sr_xFeO_3$ nanoparticles. Paramagnetic and ferromagnetic fitted magnetization *versus* magnetic field (M − H) curve at room temperature for (b) $x = 0.0$, (c) $x = 0.15$ and (d) $x = 0.25$. (e) Canted antiferromagnetic spin structures causing the net magnetic moments in Sr doped $BiFeO_3$ nanoparticles through Dzyaloshinskii-Moriya (DM) interactions.

In addition to the antiferromagnetic theory of $BiFeO_3$, we have also quantified the defects and grain boundary effects in Sr doped $BiFeO_3$ nanoparticles. The specific grain boundary area (S_{GB}) defined as the ratio of grain boundary area to volume has been discussed by Tietze *et al.*[54,55] For the dense polycrystalline sample with equiaxial grains (no pores and holes), the optimal filling grain shape is a polyhedron with 14 faces called tetrakaidecahedron and the grain boundary area to volume ratio is given as: $S_{GB} = 1.65/D$, where D is the mean grain size. In case of elongated and flattened grains, $S_{GB} = 1.65a/D$, where 'a' is the aspect ratio (ratio of grain width to grain height). The value of 'a' is less than 1 for elongated grains and greater than 1 for flattened grains. In the case of porous equiaxial polycrystalline sample, the S_{GB} value decreases approximately by the porosity coefficient P which varies from 0 for non-sintered to 1 for fully compacted polycrystals.[54,55] The average value of S_{GB} is 2.3×10^7 m^2 m^{-3} for $BiFeO_3$ nanoparticles and 2.5×10^7 m^2 m^{-3} for $Bi_{0.75}Sr_{0.25}FeO_3$ nanoparticles corresponding to an average grain size of 70 nm and 65 nm respectively. The samples are ferromagnetic only if S_{GB} exceeds a certain threshold value S_{TH}. The threshold value of S_{TH} is 1.7×10^7 m^2 m^{-3} for pure $BiFeO_3$ ceramics corresponding to average particle size of 95 nm as calculated from the data reported by Park *et al.*[11,55] These results also confirmed the enhanced ferromagnetism in Sr doped $BiFeO_3$ nanoparticles.

Table 1 Parameters extracted from fitting the magnetization hysteresis loops of $Bi_{1-x}Sr_xFeO_3$ nanoparticles

S. No.	Samples	Paramagnetic contribution $\chi \times 10^{-6}$ emu g^{-1} gauss^{-1}	Ferromagnetic contribution H_{ci} (Gauss)	M^S_{FM} (emu g^{-1})	M^R_{FM} (emu g^{-1})
1	$x = 0.00$	6.35	1300	0.0099	0.005
2	$x = 0.05$	7.4	550	0.025	0.005
3	$x = 0.10$	10.15	700	0.045	0.009
4	$x = 0.15$	9.02	480	0.085	0.0197
5	$x = 0.20$	15.6	600	0.198	0.031
6	$x = 0.25$	20.5	1100	0.72	0.22

3.6 Electron paramagnet resonance (EPR) analysis

Fig. 11 shows the room temperature EPR spectra of Sr doped $BiFeO_3$ nanoparticles. The three parameters (g-factor, asymmetry parameter P_{asy} and signal width ΔB_{p-p}) calculated from EPR measurement have been correlated with the magnetic structure of the samples. The g values were calculated by using the formula $h\nu = g\mu_B H$, where ν is operating frequency, μ_B is Bohr magneton and h is Planck's constant. The asymmetry parameter P_{asy} is defined as $P_{asy} = (1 - h_U/h_L)$ where h_U is the height of the absorption peak above the base line and h_L is the height of the absorption peak below the base line of the first derivative of the magnetic resonance absorption signal. ΔB_{p-p} is the width of the signal defined as the separation between the upper peak and the lower peak.[55–57] The calculated values of g, P_{asy} and ΔB_{p-p} are given in Table 2. Interestingly, the EPR line shifts towards lower magnetic field which gives increasing g values for $x = 0.0$ to 0.25 samples. The degree of spin canting may be calculated through vector parameter D which is defined as: $D \approx (\Delta g/g)J_{super}$, where Δg is deviation of g from value 2, J_{super} is the superexchange interaction coefficient and is assumed to be constant for all the samples. The value D is largest for $x = 0.25$ sample as seen from $\Delta g/g$ values in Table 2. This supports the M − H loop measurement results that the ferromagnetic interactions are continuously increasing with increasing Sr content in $BiFeO_3$. The high asymmetry in the EPR spectra suggested that the EPR signal is composed of two peaks. For the sake of convenience, the broad and narrow signals are designated as signal A and signal B, respectively as shown in Fig. 11(b–d) for $x = 0.0$, 0.15 and 0.20 samples. The broad and weak Gaussian signal A [H_{pp} = 2236 Gauss (peak-to-peak line width) and g-value as 2.19] and the intense and narrow Gaussian signal B [H_{pp} = 1194 Gauss and g-value as 2.04] were fitted for $x = 0.0$, 0.15 and 0.20 samples as shown in Fig. 11(b–d). The signal A is related to the ferromagnetic part and the signal B is related to the paramagnetic part.[58] The area under signal A increases continuously with increasing Sr concentration which indicates that ferromagnetic contribution increases with increasing Sr concentration in these samples.

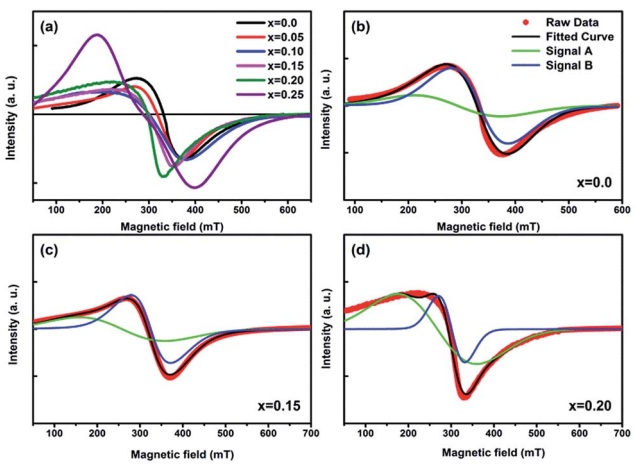

Fig. 11 Electron paramagnetic resonance (EPR) spectra of $Bi_{1-x}Sr_xFeO_3$ nanoparticles at room temperature. Fitted ESR spectra of (b) $x = 0.0$, (c) $x = 0.15$ and (d) $x = 0.20$.

3.7 Mössbauer spectroscopy

The electronic and magnetic properties of $Bi_{1-x}Sr_xFeO_3$ samples with x = 0.0, 0.10, 0.15 and 0.25 were also systematically investigated by Mössbauer spectroscopy. The Mössbauer spectrum provides valuable information about the electronic density at the nuclei (through isomer shift, IS), the possible electric field gradient (quadrupole splitting, QS) and the magnetic environment (magnetic hyperfine splitting, HF). Mössbauer spectra fitted with one doublet and one sextet for pure $BiFeO_3$ nanoparticles and fitted with one sextet for $x = 0.10$, 0.15 and 0.25 are shown in Fig. 12(a)–(d) respectively. The Mössbauer spectrum for pure $BiFeO_3$ sample is a superposition of quadrupolar doublet and magnetic sextet as shown in Fig. 12(a). This collapsed quadrupolar (doublet and sextet) spectrum is related to the particle size distribution within the synthesized sample. The tiny doublet in Mössbauer spectrum may be related to

Table 2 Calculated ESR parameters of $Bi_{1-x}Sr_xFeO_3$ nanoparticles at room temperature

S. No.	Sample	g	$\Delta g/g$	ΔB_{p-p} (Gauss)	P_{asy}
1	$x = 0.0$	2.05	0.028	1098	0.22
2	$x = 0.05$	2.12	0.06	1014	0.37
3	$x = 0.10$	2.24	0.12	1725	0.51
4	$x = 0.15$	2.25	0.125	1284	0.53
5	$x = 0.20$	2.27	0.135	1077	0.47
6	$x = 0.25$	2.35	0.175	2090	−0.09

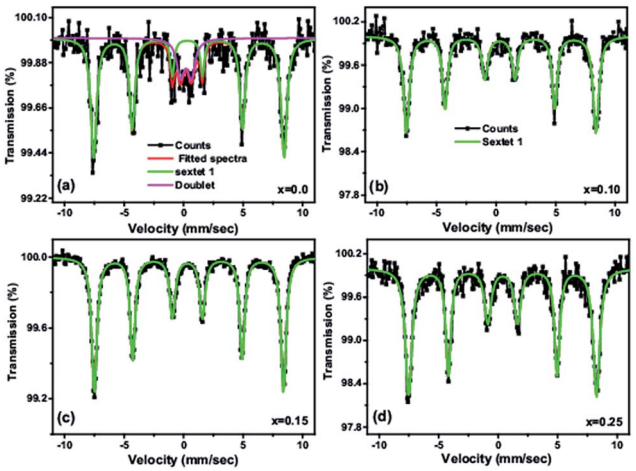

Fig. 12 Room temperature Mössbauer spectra for (a) $x = 0$, (b) $x = 0.10$, (c) $x = 0.15$ and (d) $x = 0.25$ samples fitted with one sextet.

superparamagnetic relaxation of smaller particles. Park *et al.* has reported similar type of Mössbauer spectra for $BiFeO_3$ nanoparticles of size less than 95 nm.[11] One sextet fitting hyperfine parameters are tabulated in Table 3. The isomer shift (IS) which is a measure of the oxidation state of Fe atoms is found to be ~0.37 mm s^{-1} for all the samples. The reported values of IS varies in the range 0.6–1.7 mm s^{-1} for Fe^{2+}; 0.05–0.5 mm s^{-1} for Fe^{3+} and −0.15 to 0.05 for Fe^{4+}.[59] This indicates that Fe^{3+} oxidation state is dominant in present samples. The observed values of QS are 0.1275, 0.1147, 0.1065 and −0.015 mm s^{-1} for $x = 0.0$, 0.10, 0.15 and 0.25 samples respectively. The decrease of QS with sign change on increasing Sr concentration in $BiFeO_3$ nanoparticles has been observed. This can be explained by distortion (compression) of oxygen octahedron and/or displacement of Fe ions across diagonal of pseudo-cubic crystal cell in the doped samples. Similar results have also been reported by Xiao *et al.*[60] Hyperfine magnetic field (HF) decreases from 49.70 to 49.05 Tesla with increasing Sr content for $x = 0.0$, 0.10, 0.15 and 0.25 samples. It is known that Fe^{3+} ions do not possess any orbital moment and as a consequence there is no orbital magnetism. Therefore, hyperfine magnetic field is only caused by contact Fermi interaction which is proportional to the difference of electronic densities belonging to spin-up and spin-down states. The difference appears due to polarization of the 3d electronic shell caused by interaction of Fe ion with neighbor oxygen ions. The Rietveld analysis showed that the Sr^{2+} substitution at Bi^{3+} site leads decrease in lattice parameters and creation of oxygen vacancies. Hence, the distortion in the crystal structure with increasing Sr^{2+} content results in the change of Fe ion surroundings which gives rise to the hyperfine magnetic structure. Lebeugle *et al.* reported that the spin cycloid causes the broadening of Mössbauer spectra lines.[61] The line broadening (FWHM: Full Width at Half Maximum) of the sextet decreases with increasing Sr content indicating the destruction of the spin cycloid in these samples.[60] The larger FWHM and asymmetry of intensity of the lines suggested the existence of at least two nonequivalent positions of Fe ions and therefore two sextets fitting were also done as shown in Fig. 13. The two-sextets fitting matches reasonably well with experimental data points and the obtained hyperfine parameters are shown in Table 4. A comparison of the obtained values of the parameters of hyperfine interactions with available data in the literature for iron ions with different oxygen co-ordinations indicates that two sextets with approximately equal shift of the line (IS ≈ 0.33–0.39) and small QS correspond to Fe^{3+} ions in a weakly distorted octahedral oxygen environment (Fe–O). The quadrupole splitting and hyperfine magnetic fields of the two sextets approach to each other with increasing Sr concentration in $BiFeO_3$

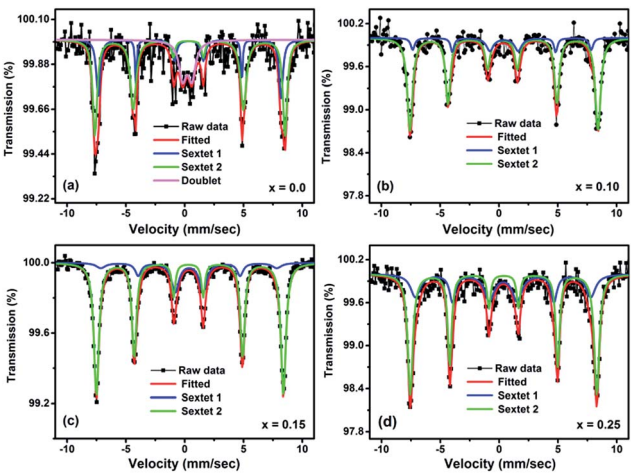

Fig. 13 Mössbauer spectra for (a) $x = 0.0$, (b) $x = 0.10$, (c) $x = 0.15$ and (d) $x = 0.25$ samples fitted with two sextets.

Table 3 Hyperfine parameters obtained from one-sextet fitting of the Mössbauer spectra: IS—Isomer Shift, QS—electric Quadrupole Splitting, HF—hyperfine magnetic field of $Bi_{1-x}Sr_xFeO_3$ nanoparticles

Sample	Type	HF (Tesla)	QS (mm s^{-1})	IS (mm s^{-1})	Area ratio
$x = 0.0$	Sextet 1	49.70	0.1275	0.377	82.01%
	Doublet		0.9069	0.1918	17.99%
$x = 0.10$	Sextet 1	49.475	0.1147	0.3694	100%
$x = 0.15$	Sextet 1	49.302	0.1065	0.3725	100%
$x = 0.25$	Sextet 1	49.05	−0.015	0.3767	100%

Table 4 Hyperfine parameters obtained from two-sextet fitting of the Mössbauer spectra: IS—Isomer Shift, QS—electric Quadrupole Splitting, HF—hyperfine magnetic field of $Bi_{1-x}Sr_xFeO_3$ nanoparticles

Sample	Type	HF (Tesla)	QS (mm s^{-1})	IS (mm s^{-1})	Area ratio
$x = 0.0$	Sextet 1	48.3006	0.0718	0.3856	25.44%
	Sextet 2	50.2383	0.1456	0.3779	56.87%
	Doublet		0.7886	0.2149	17.69%
$x = 0.10$	Sextet 1	47.1481	−0.175	0.3422	16.25%
	Sextet 2	49.6674	0.1281	0.3636	83.75%
$x = 0.15$	Sextet 1	46.5065	−0.0278	0.3626	21.81%
	Sextet 2	49.4138	0.1275	0.3761	78.19%
$x = 0.25$	Sextet 1	46.3206	−0.0164	0.3381	36.48%
	Sextet 2	49.2635	−0.0153	0.3797	63.52%

samples and this indicates the appearance of equivalence of Fe ions.

4. Conclusions

In summary, $Bi_{1-x}Sr_xFeO_3$ nanoparticles were successfully synthesized by the sol–gel route. X-ray diffraction, TEM, Raman, XPS, VSM, EPR and Mössbauer spectroscopy were applied to investigate the structure-dependent evolution of properties of perovskite $Bi_{1-x}Sr_xFeO_3$ nanoparticles. Rietveld refinement of XRD patterns suggested the coexistence of rhombohedral and pseudo tetragonal phases in 25% Sr doped $BiFeO_3$ sample. The TEM images demonstrated that particle size lies in nano range and decreases with increasing Sr concentration in $BiFeO_3$. Significant changes in intensity, position and width of $E(LO_1)$, $E(TO_2)$, $E(LO_9)$ Raman modes have been observed with increasing Sr content confirming the structural distortion. XPS spectra indicated the dominancy of Fe^{3+} oxidation state and slight increase in oxygen vacancies with increasing Sr content in $BiFeO_3$ samples. The ferromagnetic ordering component increases with increasing Sr content in $BiFeO_3$ samples due to the distorted spin structure and uncompensated surface spins which is further confirmed from EPR studies. Local magnetic behavior investigated by ^{57}Fe Mössbauer spectroscopy ruled out any valence fluctuations of Fe with Sr substitution and the hyperfine field corroborates the magnetization data. One sextet fitting of Mössbauer spectra showed changes in QS hyperfine parameter and line-width with increasing Sr content in $BiFeO_3$ nanoparticles suggesting the destruction of spin cycloid. The analysis of the spectral asymmetry demonstrated the line broadening mechanism and two sextets fitting provided further evidence for spin cycloid destruction.

Acknowledgements

Authors are thankful to Department of Science and Technology (DST) (Grant number SR/FTP/PS-91/2009) to carry out this research work. The authors are thankful to SAIF AIIMS, New Delhi and SAIF IIT, Chennai for TEM, VSM and EPR measurements. The authors are also thankful to INUP program IISc, Bangalore for Raman and FESEM measurements.

Notes and references

1 M. Fiebig, T. Lottermoser, D. Fröhlich, A. V. Goltsev and R. V. Pisarev, *Nature*, 2002, **419**, 818; M. Fiebig, *J. Phys. D: Appl. Phys.*, 2005, **38**, R123.
2 W. Eerenstein, N. D. Mathur and J. F. Scott, *Nature*, 2006, **442**, 759.
3 G. Catalan and J. F. Scott, Physics and applications of bismuth ferrite, *Adv. Mater.*, 2009, **21**, 2463–2485.
4 L. W. Martin, *Dalton Trans.*, 2010, **39**, 10813; L. W. Martin, S. P. Crane, Y.-H. Chu, M. B. Holcomb, M. Gajek, M. Huijben, C.-H. Yang, N. Balke and R. Ramesh, *J. Phys.: Condens. Matter*, 2008, **20**, 434220.
5 Y. Li, M.-S. Cao, D.-W. Wang and J. Yuan, *RSC Adv.*, 2015, **5**, 77184.
6 B. Sun, Y. Liu, W. Zhao and P. Chen, *RSC Adv.*, 2015, **5**, 13513.
7 S. Das, S. Rana, S. M. Mursalin, P. Rana and A. Sen, *Sens. Actuators, B*, 2015, **218**, 122.
8 D. Tiwari, D. J. Fermin, T. K. Chaudhuri and A. Ray, *J. Phys. Chem. C*, 2015, **119**, 5872; S. Acharya, S. Martha, P. C. Sahoo and K. Parida, *Inorg. Chem. Front.*, 2015, **2**, 807.
9 A. Rogov, M. Irondelle, F. Ramos-Gomez, J. Bode, D. Staedler, S. Passemard, S. Courvoisier, Y. Yamamoto, F. Waharte, D. Ciepielewski, P. Rideau, S. Gerber-Lemaire, F. Alves, J. Salamero, L. Bonacina and J.-P. Wolf, *ACS Photonics*, 2015, **2**(10), 1416.
10 M. Escobar Castillo, V. V. Shvartsman, D. Gobeljic, Y. Gao, J. Landers, H. Wende and D. C. Lupascu, *Nanotechnology*, 2013, **24**, 355701.
11 T. J. Park, G. C. Papaefthymiou, A. J. Viescas, A. R. Moodenbaugh and S. S. Wong, *Nano Lett.*, 2007, **7**, 766.
12 C.-H. Yang, D. Kan, I. Takeuchi, V. Nagarajan and J. Seidel, *Phys. Chem. Chem. Phys.*, 2012, **14**, 15953.
13 B. Bhushan, A. Basumallick, S. K. Bandopadhyay, N. Y. Vasanthacharya and D. Das, *J. Phys. D: Appl. Phys.*, 2009, **42**(6), 065004.
14 P. K. Jha, P. A. Jha, P. Kumar, K. Asokan and R. K. Dwivedi, *J. Alloys Compd.*, 2016, **667**, 178; Z. X. Cheng, X. L. Wang, Y. Du and S. X. Dou, *J. Phys. D: Appl. Phys.*, 2010, **43**, 242001.
15 D. C. Arnold, *IEEE Trans. Ultrason. Eng.*, 2015, **62**, 62, DOI: 10.1109/tuffc.2014.006668.
16 J. Zhao, S. Liu, W. Zhang, Z. Liu and Z. Liu, *J. Nanopart. Res.*, 2013, **15**, 1969, DOI: 10.1007/s11051-013-1969-7; T. Karthik, T. Durga Rao, A. Srinivas and S. Asthana, *J. Mater. Sci.: Mater. Electron.*, 2015, **26**, 8676.
17 W. W. Mao, X. F. Wang, Y. M. Han, X. A. Li, Y. T. Li, Y. F. Wang, Y. W. Ma, X. M. Feng, T. Yang, J. Yang and W. Huang, *J. Alloys Compd.*, 2014, **584**, 520; W. W. Mao, X. F. Wang, L. Chu, Y. Y. Zhu, Q. Wang, J. Zhang, J. Yang, X. A. Li and W. Huang, *Phys. Chem. Chem. Phys.*, 2016, **18**, 6399.
18 B. Wang, S. Wang, L. Gong and Z. Zhou, *Ceram. Int.*, 2012, **38**, 6643.
19 S. Hussain, S. K. Hasanain, G. H. Jaffari, N. Z. Ali, M. Siddique and S. I. Shah, *J. Alloys Compd.*, 2015, **622**, 8; T. Hussain, S. A. Siddiqi, S. Atiq and M. S. Awan, *Prog. Nat. Sci.*, 2013, **23**, 487.
20 B. Bhushan, A. Basumallick, N. Y. Vasanthacharya, S. Kumar and D. Das, *Solid State Sci.*, 2010, **12**, 1063.
21 B. Kundys, A. Maignan, C. Martin, N. Nguyen and C. Simon, *Appl. Phys. Lett.*, 2008, **92**, 112905.
22 K. Balamurugan, N. H. Kumar and P. N. Santhosh, *J. Appl. Phys.*, 2009, **105**, 07D909.
23 J. Li, Y. Duan, H. He and D. Song, *J. Alloys Compd.*, 2001, **315**, 259.
24 S. K. Mandal, T. Rakshit, S. K. Ray, S. K. Mishra, P. S. R. Krishna and A. Chandra, *J. Phys.: Condens. Matter*, 2013, **25**, 055303.
25 X. Wang, S. Y. Wang, W. F. Liu, F. Guo, X. J. Xi, H. J. Wang and D. J. Li, *Mod. Phys. Lett. B*, 2014, **28**(7), 1450050.
26 S. Gosh, S. Das Gupta, A. Sen and H. S. Maiti, *J. Am. Ceram. Soc.*, 2005, **88**(5), 1349–1352; M. Arora, P. C. Sati, S. Chauhan,

S. Chhoker, A. K. Panwar and M. Kumar, *J. Supercond. Novel Magn.*, 2013, **26**, 443.
27 H. D. Megaw and C. N. W. Darlington, *Acta Crystallogr., Sect. A: Cryst. Phys., Diffr., Theor. Gen. Crystallogr.*, 1975, **31**, 161.
28 S. M. Selbach, T. Tybell, M. A. Einarsrud and T. Grande, *Chem. Mater.*, 2007, **19**, 6478.
29 J. Rodriguez-Carvajal, *FullProf: A Rietveld Refinement and Pattern Matching Analysis Program (Version: April 2008)*, Laboratoire Léon Brillouin (CEA-CNRS), France, 2000.
30 S. Diodati, L. Nodari, M. M. Natile, U. Russo, E. Tondello, L. Lutterotti and S. Gross, *Dalton Trans.*, 2012, **41**, 5517.
31 J. A. Alonso, M. J. Martínez-Lope, J. L. García-Muñoz and M. T. Fernández-Díaz, *J. Phys.: Condens. Matter*, 1997, **9**, 6417.
32 P. Hermet, M. Goffinet, J. Kreisel and P. Ghosez, *Phys. Rev. B: Condens. Matter Mater. Phys.*, 2007, **75**, 220102.
33 P. Chen, X. Xu, C. Koenigsmann, A. C. Santulli, S. S. Wong and J. L. Musfeldt, *Nano Lett.*, 2010, **10**, 4526.
34 A. A. Porporati, K. Tsuji, M. Valant, A. K. Axelsson and G. Pezzotti, *J. Raman Spectrosc.*, 2010, **41**, 84.
35 J. Bielecki, P. Svedlindh, D. T. Tibebu, S. Cai, S.-G. Eriksson, L. Börjesson and C. S. Knee, *Phys. Rev. B: Condens. Matter Mater. Phys.*, 2012, **86**, 184422.
36 M. Cazayous, D. Malka, D. Lebeugle and D. Colson, *Appl. Phys. Lett.*, 2007, **91**, 071910.
37 J.-P. Zhou, R.-J. Xiao, Y.-X. Zhang, Z. Shi and G.-Q. Zhu, *J. Mater. Chem. C*, 2015, **3**, 6924.
38 D. Varshney and A. Kumar, *J. Mol. Struct.*, 2013, **1038**, 242.
39 N. Suzuki and H. Kamimura, *J. Phys. Soc. Jpn.*, 1973, **35**, 985.
40 J. Hlinka, J. Pokorny, S. Karimi and I. M. Reaney, *Phys. Rev. B: Condens. Matter Mater. Phys.*, 2011, **83**, 020101.
41 M. O. Ramirez, M. Krishnamurthi, S. Denev, A. Kumar, S. Y. Yang, Y. H. Chu, E. Saiz, J. Seidel, A. P. Pyatakov, A. Bush, D. Viehland, J. Orenstein, R. Ramesh and V. Gopalan, *Appl. Phys. Lett.*, 2008, **92**, 022511.
42 P. Kumar, N. Shankhwar, A. Srinivasan and M. Kar, *J. Appl. Phys.*, 2015, **117**, 194103.
43 M. Sakar, S. Balakumar, P. Saravanan and S. Bharathkumar, *Nanoscale*, 2015, **7**, 10667.
44 Z. Quan, W. Liu, H. Hu, S. Xu, B. Sebo, G. Fang, M. Li and X. Zhao, *J. Appl. Phys.*, 2008, **104**, 084106.
45 A. Tamilselvan, S. Balakumar, M. Sakar, C. Nayek, P. Murugavel and K. S. Kumar, *Dalton Trans.*, 2014, **43**, 5731.
46 Q.-H. Wu, M. Lin and W. Jaegermann, *Mater. Lett.*, 2005, **59**, 1980–1983.
47 D. Mazumdar, R. Knut, F. Thöle, M. Gorgoi, S. Faleev, O. N. Mryasov, V. Shelke, C. Ederer, N. A. Spaldin, A. Gupta and O. Karis, *J. Electron Spectrosc. Relat. Phenom.*, 2016, **208**, 63.
48 P. Kumar, P. Pal, A. K. Shukla, J. J. Pulikkotil and A. Dogra, *Phys. Rev. B: Condens. Matter Mater. Phys.*, 2015, **91**, 115127.
49 H. Zhang, W. Liu, P. Wu, M. Guo, X. Xu, X. Xi, J. Gao, G. Rao and S. Wang, *J. Mater. Chem. C*, 2015, **3**, 4141.
50 L. R. Shah, H. Zhu, W. G. Wang, B. Ali, T. Zhu, X. Fan, Y. Q. Song, Q. Y. Wen, H. W. Zhang, S. I. Shah and J. Q. Xiao, *J. Phys. D: Appl. Phys.*, 2010, **43**, 035002.
51 F. Huang, Z. Wang, X. Lu, J. Zhang, K. Min, W. Lin, R. Ti, T. T. Xu, J. He, C. Yue and J. Zhu, *Sci. Rep.*, 2013, **3**, 2907.
52 S.-Z. Lu and X. Qi, *J. Am. Ceram. Soc.*, 2014, **97**(7), 2185.
53 H. Feng, *J. Magn. Magn. Mater.*, 2010, **322**, 1765.
54 T. Tietze, *et al.*, *Sci. Rep.*, 2015, **5**, 8871.
55 S. Chauhan, M. Kumar, S. Chhoker and S. C. Katyal, *J. Alloys Compd.*, 2016, **666**, 454.
56 D. Maurya, H. Thota, A. Garg, B. Pandey, P. Chand and H. C. Verma, *J. Phys.: Condens. Matter*, 2009, **21**, 026007.
57 M. Arora, P. C. Sati, S. Chauhan, M. Kumar and S. Chhoker, *Mater. Lett.*, 2014, **132**, 327; S. Chauhan, M. Kumar, S. Chhoker, S. C. Katyal and M. Singh, *RSC Adv.*, 2016, **6**, 43080.
58 D. Karmakar, S. K. Mandal, R. M. Kadam, P. L. Paulose, A. K. Rajarajan, T. K. Nath, A. K. Das, I. Dasgupta and G. P. Das, *Phys. Rev. B: Condens. Matter Mater. Phys.*, 2007, **75**, 144404.
59 N. N. Greenwood and T. C. Gibb, *Mössbauer Spectroscopy*, Chapman and Hall London, 1971.
60 R. Xiao, V. O. Pelenovich and D. Fu, *Appl. Phys. Lett.*, 2013, **103**, 012901.
61 D. Lebeugle, D. Colson, A. Forget, M. Viret, P. Bonville, J. F. Marucco and S. Fusil, *Phys. Rev. B: Condens. Matter Mater. Phys.*, 2007, **76**, 024116.

